DTU Library

Trajectory surface-hopping photoinduced dynamics from Rydberg states of trimethylamine

Pápai, Mátyás Imre; Li, Xusong; Nielsen, Martin M.; Møller, Klaus Braagaard

PCCP

Physical Chemistry Chemical Physics

Accepted Manuscript

Volume 19
Number 1
7 January 2017
Pages 1-896

PCCP

Physical Chemistry Chemical Physics

rsc.li/pccp

ISSN 1463-9076

PAPER
H.-P. Loock et al.
Determination of the thermal, oxidative and photochemical
degradation rates of scintillator liquid by fluorescence EEM
spectroscopy.

ROYAL SOCIETY
OF CHEMISTRY

rsc.li/pccp

PCCP

ARTICLE TYPE

Trajectory surface-hopping photoinduced dynamics from Rydberg states of trimethylamine[†]

Mátyás Pápai,[*a,b] Xusong Li,[a,c] Martin M. Nielsen,[d] and Klaus B. Møller[a]

We present a computational study on nonadiabatic excited-state dynamics initiated from the $3p$ Rydberg states of trimethylamine (TMA). We utilise a methodology based on full-dimensional (39 D) trajectory surface-hopping (TSH) simulations, in which propagation is carried out on on-the-fly density functional theory (DFT)/time-dependent DFT (TD-DFT) potentials. Both our electronic structure benchmarks to high-level *ab initio* methods (EOM-CCSD, CASPT2) and TSH simulations demonstrate high-accuracy of the applied CAM-B3LYP functional for the description of Rydberg excited states. Based on our excited-state simulations, we construct the following mechanistic picture: when pumped resonantly to the $3p$ Rydberg manifold, TMA coherently vibrates along the planarisation mode with a period of 104 fs and an exponential coherence decay time constant of 240 fs. Nonadiabatic dynamics occur on a faster (~ 1 ps) and a slower (~ 3 ps) timescale, along the N-C stretching mode by mixing with a dissociative σ^*_{N-C} state. As a minor relaxation channel, $3p \rightarrow 3s$ internal conversion occurs via branching at the $\sigma^*_{N-C}/3s$ intersection. We find that photodissociaton is hardly observable within 3 ps (1%), which is a failure of the range-separated hybrid CAM-B3LYP functional, as a consequence of its static electron correlation deficiency at long range. In contrast, pure DFT (GGA-BLYP) provides an accurate long-range description (19 % dissociation yield), also supported by comparison to recent ultrafast experiments, even if the Rydberg state energies are significantly underestimated (> 1 eV). Finally, we reveal the crucial role of vibrational coherence and energy transfer from the planarisation mode for N-C bond activation and resulting nonadiabatic dynamics. The present work illustrates the importance of nuclear-electronic coupling for excited-state dynamics and branching at conical intersections.

1 Introduction

Ultrafast excited-state dynamics have received great attention in the past decades due to their vital role in fundamental and applied research fields, such as photochemistry,[1] solar energy conversion,[2,3] and molecular data storage.[4,5] Excited-state simulations constitute a powerful toolbox to obtain a thorough understanding and complement ultrafast experiments. The most rigorous theoretical approach for these simulations is the framework of quantum dynamics (QD), i.e., solution to the molecular time-dependent Schrödinger equation. While this leads to the numerically exact solution, exponential scaling with the number of nu-

clear degrees of freedom (DoF) limits QD to be applicable only to very small molecules (≤ 6 DoF). For multidimensional problems, advanced numerical QD methods, such as the multiconfiguration time-dependent Hartee (MCTDH) method,[6,7] exist, but still suffer from the dimensionality bottleneck, even if it is slightly alleviated to treat 10–20 DoF. An alternative and complementary technique is based on semiclassical trajectories, which enables the treatment of the complete nuclear configurational space. However, the price to pay is the lack of rigorous description of quantum effects, such as nonadiabatic transitions, interferences, and tunneling.

Excited-state dynamics very often involve electronic transitions, such as internal conversion (IC, no spin change) and intersystem crossing (ISC, spin transition due to spin-orbit coupling). These dynamics occur in the vicinity of conical intersections (CIs) and surface crossings, where the Born-Oppenheimer approximation breaks down, as the nuclear-electronic (nonadiabatic) coupling becomes non-negligible. Nonadiabatic effects are essentially treated correctly by QD but not by classical dynamics. The latter can be extended by describing nonadiabatic transitions as stochastic hops between potential energy surfaces (PESs), leading to the term trajectory surface hopping (TSH).[8]

[a] *Department of Chemistry, Technical University of Denmark, Kemitorvet 207, DK-2800 Kongens Lyngby, Denmark. E-mail: papai@kemi.dtu.dk.*
[b] *Present address: Wigner Research Centre for Physics, P.O. Box 49, H-1525 Budapest, Hungary.*
[c] *CAS Key Laboratory of Biobased Materials, Qingdao Institute of Bioenergy and Bioprocess Technology, Chinese Academy of Sciences, Qingdao 266101, China.*
[d] *Department of Physics, Technical University of Denmark, Fysikvej 307, DK-2800 Kongens Lyngby, Denmark.*
† Electronic Supplementary Information (ESI) available: animation of the most important normal modes in MPEG format. See DOI: 10.1039/cXCP00000x/...

Here the nuclear wavepacket is approximated by a swarm of classical trajectories and hopping between different electronic states is allowed; thus, certain quantum effects, such as wavepacket splitting can be accounted for. However, there is no guarantee that the simulation converges to the correct quantum solution, even if all possible trajectories could be considered. Nevertheless, TSH has been successful to simulate the excited-state dynamics of various molecules including small organic model systems,[9,10] nucleobases,[11,12] and even transition metal complexes,[13–15] the results in reasonable agreement with those of ultrafast experiments. Furthermore, TSH is well-suited for processes accompanied by large structural changes, such as bond dissociation and photochemical reactions, and energy transfer, i.e., internal vibrational energy redistribution (IVR) and vibrational coooling. This is a clear advantage over QD, for which a modified Hamiltonian is necessary from the widely-utilised vibronic-coupling model using normal modes.

Excited states possessing Rydberg character, typically observable for small organic molecules, are electronic states whose excited electron is highly diffuse, converging to the ionised cationic state. Ultrafast excited-state dynamics between Rydberg states are intriguing, as their PESs are parallel, separated by a significant energy gap for the Rydberg series (s, p, d, etc.); this questions how IC can occur between Rydberg states. A prototype for such dynamics is the case of the trimethylamine (TMA) molecule (Figure 1). Upon excitation into the $3p$ Rydberg manifold at 208 nm, Cardoza et $al.$ found IC into the $3s$ state with a time constant of 2.9 ± 0.2 ps, as determined by gas-phase ionisation electron spectroscopy.[16] The authors did not observe photodissociation of TMA. In a recent time-resolved X-ray scattering experiment, pumped at 200 nm, Ruddock et $al.$ reported branching photodissociation dynamics, with a major slow 74 ± 6 ps and a minor fast 640 ± 130 fs component.[17] Onitsuka et $al.$ performed ion-imaging experiments on TMA, from which they concluded that the photodissociation yield is highly sensitive to the excitation wavelength in the 200–236 nm region.[18] These results indicate that photodissociation also occurs upon excitation to the $3s$ Rydberg state, but the yield is several times smaller, relative to the case when the $3p$ excitation dominates. In this work, we present a TSH study on the excited-state dynamics of TMA, promoted to the $3p$ Rydberg manifold. Our goal is twofold: i) to complement the quoted time-resolved experiments, and ii) analyse the applicability of TSH to dynamics initiated and involving Rydberg states.

2 Computational methodology

2.1 Electronic structure calculations

In all electronic structure calculations, we utilise the aug-cc-pVDZ basis set; the included diffuse functions are essential for the description of Rydberg states. In the present work, we only consider singlet states. The ground and excited-state geometries were fully optimised using the density functional theory (DFT) CAM-B3LYP[19]/aug-cc-pVDZ method, and its time-dependent DFT (TD-DFT) variant, for the excited states. We selected CAM-B3LYP based on its known accuracy for Rydberg states.[20,21] Harmonic vibrational frequencies were calculated to ensure that the opti-
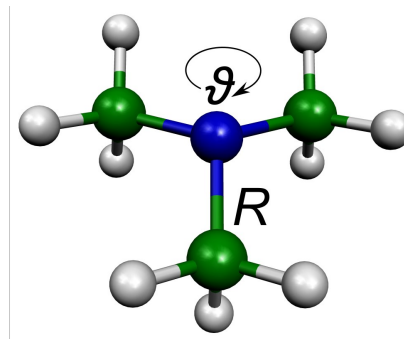

Fig. 1 Molecular pyramidal structure of the TMA molecule in its electronic ground state. Also depicted are the two key nuclear coordinates of the molecule: the N-C bond length R and the C-C-C-N dihedral angle ϑ (umbrella angle).

mised geometry corresponds to a true minimum on the given potential energy surface (PES). At the optimised ground-state geometry, i.e., the Franck-Condon (FC) geometry, we assess the performance of different quantum chemical methods for vertical excitations to the Rydberg states. In addition to CAM-B3LYP, we employ equation-of-motion coupled cluster with singles and doubles (EOM-CCSD), complete active space self-consistent field (CASSCF), and multiconfigurational second-order perturbation theory (CASPT2). For DFT/TD-DFT and EOM-CCSD we approximate two electron integrals using the split resolution of identity (RI-J) and chain of sphere (COSX) methods. In the TD-DFT computations, we employ the Tamm-Dancoff approximation (TDA).[22] For CASSCF, we constructed an active space, in which 6 electrons were distributed on 14 active orbitals (6e,14o). The 14 active orbitals are the orbitals required to describe i) the Rydberg excited states: the nitrogen lone pair (n), the $3s$, $3p_x$, $3p_y$, and $3p_z$ Rydberg (Ryd) orbitals, ii) N-C bond dissociation for the calculations of potential energy surfaces (PESs) along the N-C stretching coordinate: the two lowest bonding σ_{N-C} and correlating antibonding σ^*_{N-C} orbitals, and iii) 5 additional orbitals required to maintain the active space at elongated N-C distances, with N-$3d_{xz}$, N-$3s$/N-$3d_{z^2}$ (Ryd), and three orbitals with N-$4s$/H-$3s$ (Ryd) character. The CASSCF calculations were averaged over 10 states. In the CASPT2 calculations, we froze the N-$1s$ and C-$1s$ core orbitals and applied an imaginary level shift of 0.2 a.u. to eliminate intruder states. We set the IPEA shift (shift to the zeroth-order Hamiltonian, with a default value of 0.25 a.u.) to zero, as it was found that its use is not justified and not beneficial for the excited states of organic molecules.[23] We performed multi-state MS-CASPT2 calculations for 10 states.

For the calculation of one-dimesional DFT/TD-DFT and CASPT2 PESs, we generated structures from the CAM-B3LYP-optimised geometry of the ground state and the lowest singlet excited state (S_1). These structures were obtained by varying a single nuclear coordinate while keeping all the others fixed. We here note that throughout this article we use two notations for electronic states: i) adiabatic, based on the energetic order (S_0, S_1, S_2, etc.), and ii) electronic character – (GS, Ryd, etc.). For instance, the character of the adiabatic S_1 state at the FC and optimised S_1 geometry is Ryd-$3s$, but the character may and will vary,

as seen later, depending on the nuclear geometry. We calculate two types of PESs: relaxed, in which case all nuclear coordinates except the scanned one, at each point, are optimised for the given electronic state (in this work, S_0 or S_1); and rigid, here only a single point calculation is performed at each geometry.

All electronic structure calculations were carried out using the ORCA4.2 quantum chemistry package,[24,25] with the exception of the CASSCF/CASPT2 computations, for which we utilised Open-Molcas18.09.[26,27]

2.2 Nonadiabatic dynamics simulations

This work is centered on the excited-state dynamics of TMA. We employ a framework of full-dimensional (39 D) TSH. As TSH nowadays is a standard method for nonadiabatic dynamics, we summarise the method only briefly, and for details, refer to the literature.[8,28] In TSH, the nuclei are propagated classically, by solving Newton's equations of motion; the nuclear motion is dictated by the forces, which are determined by quantum chemistry, through solution to the time-independent electronic Schrödinger equation within the Born-Oppenheimer approximation. Nonadiabatic transitions are approximated by stochastic hops between PESs during the propagation of trajectories. The hopping probability is proportional to the nonadiabatic coupling, which is large when the energy gap between two electronic states is small, i.e., in the vicinity of conical intersections and avoided crossings. The electronic wave function is expressed as linear combination of electronic basis states, whose coefficients are propagated according to the time-dependent electronic Schrödinger equation.

We follow Tully's fewest switches scheme,[29] which minimises the number of hops in a Δt time step, to calculate the hopping probabilities. For these probabilities and electronic propagation, we utilise wave function overlaps (local diabatisation[30,31]), which circumvents the often complicated computation of nonadiabatic coupling vectors, and is numerically more stable than propagation by nonadiabatic couplings. We utilise a $\Delta t = 0.5$ fs and 0.005 fs for nuclear and electronic propagation, respectively. For the nuclear propagation, we integrated Newton's second law using a Velocity Verlet algorithm. We perform the TSH simulations within the adiabatic electronic basis (MCH = molecular Coulombic Hamiltonian, as no external couplings, such as spin-orbit couplings, or couplings with an electric field, are present), for 5 singlet states (GS) plus the lowest 4 excited states. We account for quantum decoherence correction using the energy-based scheme of Granucci et al. with a decoherence (exponential damping) parameter equal to 0.1 a.u.[32] We generated 200 initial conditions sampled from a Wigner distribution based on the ground-state normal modes. We used a stochastic algorithm to determine the initial electronic state, based on excitation energies and oscillator strengths calculated at the sampled geometries. Here, we applied an energy window that allows all GS $\rightarrow 3p$ excitations, but no GS $\rightarrow 3s$. This led to the selection of 156 initial conditions, for which we ran the trajectories for 3 ps.

We propagate the trajectories on on-the-fly DFT/TD-DFT potentials. We made this choice based on the reliability of CAM-B3LYP for Rydberg states[20,21] and the results presented in Sec-

tions 3.1 and 3.2. It is known that the DFT/TD-DFT description of conical intersections involving the electronic ground state is problematic due to the fact that it is referenced to a single Slater determinant.[28,33] In our simulations, such intersections are approached, and we indeed observed failure to converge DFT in these situations. We overcome this deficiency by forcing an irreversible hop to the S_0 whenever the S_1-S_0 energy gap is smaller or equals 0.15 eV. This value is based on our recent TSH study of a ring-opening reaction, for which forcing the hops to S_0 with 0.15 eV threshold led to reliable dynamics, in comparison to CASSCF TSH simulations and time-resolved experimental data.[34] For reasons detailed later, we performed a second set of TSH simulations using the pure (GGA) BLYP exchange-correlation functional[35,36] both for generating the initial conditions (Wigner distribution) and propagating the trajectories.

All TSH simulations were carried out using the SHARC2.1[37–39] program with the SHARC-ORCA interface, to couple the on-the-fly electronic structure calculations to the propagation of trajectories.

2.3 Normal mode analysis

In order to study the structural and energy flow dynamics, we carry out a normal mode analysis on the obtained trajectories. This is realised by projecting the Cartesian nuclear displacements from the FC geometry and Cartesian velocities onto the GS normal modes. The normal mode matrix $\boldsymbol{D}$ is obtained by diagonalisation of the mass-weighted Hessian matrix; then, the mass-weighted normal mode coordinates and velocities are calculated as:

$$\boldsymbol{q}(t) = \boldsymbol{D}^T \Delta \boldsymbol{r}(t) \qquad (1)$$

$$\dot{\boldsymbol{q}}(t) = \boldsymbol{D}^T \boldsymbol{v}(t) , \qquad (2)$$

with $\Delta \boldsymbol{r}(t)$ and $\boldsymbol{v}(t)$ being the time-dependent Cartesian nuclear displacements and velocities, respectively; $\boldsymbol{q}(t)$ and $\dot{\boldsymbol{q}}(t)$ are the time-dependent mass-weighted normal mode coordinates and velocities, respectively. Finally, we calculate the average nuclear coordinates and kinetic energies by averaging $q_i(t)$ and $\dot{q}_i^2(t)/2$, where i runs over the normal modes, over all trajectories. Note that by construction, this projection technique separates translational and rotational motion from vibrations. We also mention that normal mode here are only used as a projection technique, thus energy transfer between the modes is possible (in the TSH simulations, energy dissipation is allowed).

3 Results and discussion

As the underlying electronic structure is decisive for excited-state simulations, in Sections 3.1 and 3.2, we explore the relevant electronic states of TMA using quantum chemistry. Afterwards, we present and analyse the results of TSH simulations in Sections $3.3 - 3.6$.
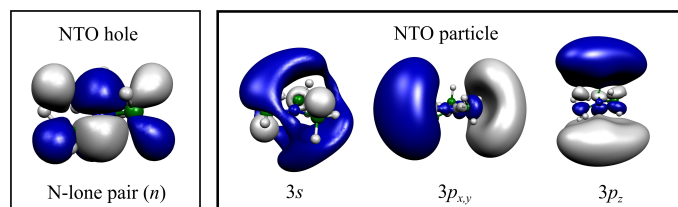
Fig. 2 Natural transition orbitals (NTOs) of the Rydberg excited states. Calculated at the $3s$ (S$_1$) equilibrium geometry at the TD-CAM-B3LYP/aug-cc-pVDZ level of theory. All 4 excited states are purely described by a single $n \to$ Ryd transition.

3.1 Vertical excitations and optimised geometries of the Rydberg states

The four lowest-lying excited states of TMA at its equilibrium ground-state geometry are the Rydberg $3s$, $3p_x$, $3p_y$, and $3p_z$ states. Table 1 compares the excitation energies and oscillator strengths, calculated at various levels of theory, at the CAM-B3LYP/aug-cc-pVDZ-optimised GS geometry, to experimental values.

The TD-DFT, EOM-CCSD, and MS-CASPT2(6e,14o)-calculated excitation energies are in excellent agreement with each other, as well as the experimental values; this evidences accurate description of the excited states at the Franck-Condon (FC) geometry. For state-averaged CASSCF, ca. 1 eV lower excitation energies are obtained, which is attributed to the lack of dynamical electron correlation. Importantly, all calculated $3p - 3s$ energy gaps are in good agreement, with a largest discrepancy of ca. 0.25 eV. We note that the excitation energies can be considered to be converged with respect to the applied basis set, differences between aug-cc-pVDZ and aug-cc-pVTZ-calculated values, even for EOM-CCSD, are below 0.1 eV. The ratio of $3s/3p$ oscillator strengths are in good agreement with the experimental absorption strengths, identifying the absorption maximum as transition to $3p_z$ and a one order of magnitude smaller contribution from $3s$.

The R(N-C) and ϑ values corresponding to the DFT-optimised structures of the GS and excited states are given in Table 2. In its electronic ground state, TMA has a trigonal pyramidal structure due to the repulsion of the N-lone pair and the electrons in N-C bonds. This is well-reproduced by the DFT GS optimisation, yielding $\vartheta = 32.1$ deg. In case of the $3s$ and $3p_{x,y}$ Rydberg excited states, the optimised structures are planar, i.e., $\vartheta \sim 0$ deg. This is due to the fact that in these states, an electron is excited from the nitrogen lone pair (n) to a Rydberg orbital (see the natural transition orbitals in Figure 2), which lifts the repulsion interaction. In the case of the $3p_z$ Rydberg state, the structure is less planar ($\vartheta = 9.6$ deg.) The differences between the optimised excited and ground-state structures are dominated by the ϑ-planarisation, all other changes, including the N-C stretching are smaller. Comparison of the energies of the optimised excited-state structures (Table 2) to the vertical excitations at the FC geometry (Table 1) reveals ca. $0.6 - 0.8$ eV reorganization, mainly attributed to the ϑ-relaxation.

3.2 Ground and excited-state potential energy curves

As the dynamics occur on potential energy surfaces along distortions from the FC geometry, we here explore the relevant ground and excited-state PESs.

Above, we identified ϑ to account for the main changes between the optimised ground and excited-state structures, thus, we first discuss the PESs along ϑ. Fig. 3 presents the DFT/TD-DFT (CAM-B3LYP) PESs along ϑ, relaxed in the adiabatic S$_1$ state. We note that relaxation to the ground state and the other excited states results in rather similar PESs. The ground-state PES is a double-well potential, i.e., two minima at ± 32 deg. connected by a saddle point at $\vartheta = 0$ deg. with a barrier of 0.31 eV, in agreement with amine inversion. The excited-state PESs clearly show the characteristics of Rydberg states: parallel potentials without any crossings and a large $3s$-$3p$ separation (ca. 0.9-1.0 eV around $\vartheta = 0$ deg.), the $3p_{x,y} - 3p_z$ gap is much smaller (ca. 0.1 eV). The Rydberg potentials are flat around their minima, which are centered around $\vartheta = 0$ deg., consistent with GS $\to$ Ryd excitation (for S$_4$-$3p_z$, two very shallow minima exist, slightly shifted from the perfectly planar geometry). The Rydberg PESs exhibit significant nuclear gradient at the FC point, forecasting strong planarisation dynamics upon GS $\to$ Ryd excitation.
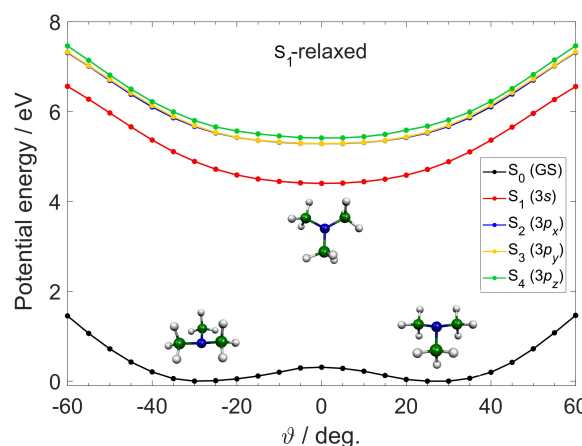

Fig. 3 Adiabatic PESs along ϑ, relaxed in the S$_1$ state ($R \sim 1.43$ Å). Calculated at the CAM-B3LYP/aug-cc-pVDZ level of theory. The pyramidal and planar structures of TMA are also shown. Due to degeneracy, to the blue curve is hidden behind the yellow one.

Figure 3 also reveals that the Rydberg character of the excited states is preserved along ϑ, which is the reason for the absence of surface crossings. It is known for alkyl and cyclic amines, however, that dissociative states can mix into Rydberg states at elongated N-C distances.[20,21] To investigate this, we calculated the PESs of TMA along the R(N-C) stretching coordinate. Fig. 4 displays the CAM-B3LYP potentials along R, relaxed in the ground state, a situation which occurs during the very initial dynamics. Importantly, the S$_2$/S$_1$ potentials exhibit an intersection at $R = 1.8$ Å (appearing as an avoided crossing in the 1D adiabatic potentials; a similar but less apparent crossing for the S$_3$/S$_2$ states appears at $R = 1.7$ Å). These intersections are due to mixing of the dissociative $n \to \sigma^*_{N-C}$ state into the Rydberg states. As R elongates, the antibonding σ^*_{N-C} orbital, depicted in Fig. 5, is

Physical Chemistry Chemical Physics Accepted Manuscript

Table 1 Excitation energies (eV) from the electronic ground state to the four lowest-lying Rydberg states. Calculated at the CAM-B3LYP-optimised GS geometry using the aug-cc-pVDZ basis set. In parantheses, the calculated oscillator strengths are given. The experimental absorption intensities were scaled to match the oscillator strengths. The shown experimental values were taken from refs 40 and 41.

Excitation	TD-CAM-B3LYP	EOM-CCSD	SA-CASSCF(6e,14o)	MS-CASPT2(6e,14o)	Exp.
$3s$ (S_1)	5.359 (0.020)	5.357 (0.021)	4.583 (0.017)	5.482 (0.014)	5.460 (0.018)
$3p_x$ (S_2)	6.100 (0.002)	6.101 (0.004)	5.182 (0.001)	6.243 (0.009)	−
$3p_y$ (S_3)	6.109 (0.002)	6.101 (0.004)	5.192 (0.001)	6.244 (0.009)	−
$3p_z$ (S_4)	6.221 (0.119)	6.155 (0.108)	5.239 (0.172)	6.280 (0.097)	6.229 (0.130)

Table 2 Key structural parameters obtained from the DFT geometry optimizations carried out at the CAM-B3LYP/aug-cc-pVDZ level of theory.

State	R (Å)	ϑ (deg.)	Energy (eV)
GS (S_0)	1.449	32.1	0.000
$3s$ (S_1)	1.434	0.0	4.600
$3p_x$ (S_2)	1.433	0.0	5.471
$3p_y$ (S_3)	1.433	0.1	5.471
$3p_z$ (S_4)	1.443	9.6	5.605

Fig. 5 NTOs illustrating the dissociative $n \rightarrow \sigma^*$ character. Calculated for the S_2 state at the S_0-relaxed $R = 1.8$ Å geometry. This excited state is purely described by a single $n \rightarrow \sigma^*$ transition.

lowered, which allows the dissociative state to couple with the Rydberg states. Analysis of the electronic excitation characters reveals $\sigma^*/3s$ and $\sigma^*/3p_x$ coupling characters, at $R = 1.8$ Å and 1.7 Å, respectively. All S_0-relaxed potentials show dissociative character at large N-C distances, but the flattening of the curves is rather slow.
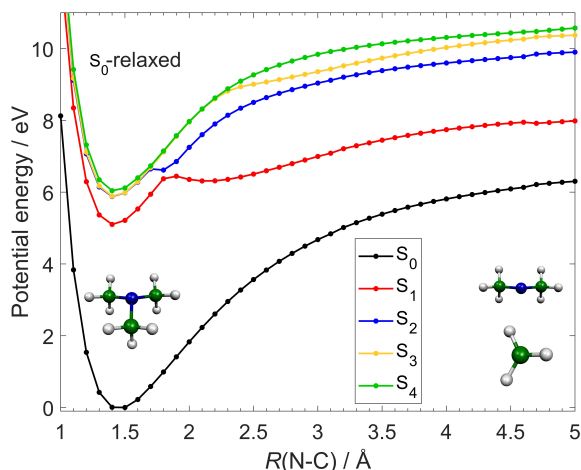

Fig. 4 Adiabatic PESs along R, relaxed in the S_0 state ($\vartheta \sim 32$ deg.). Calculated at the CAM-B3LYP/aug-cc-pVDZ level of theory. The optimised structures at $R = 1.5$ Å and 5.0 Å are also shown.

As discussed above, the S_0-relaxed excited-state PESs along R interact via the dissociative $n \rightarrow \sigma^*_{N-C}$ state (abbreviated hereafter as the σ^* state). However, it is also clear from Fig. 4 that the ground state does not couple to the excited states. This S_0-relaxed picture is though only valid for the very initial dynamics (up to, at most ca. 100 fs); below, we show that when the structure adapts to the electronic excitation, significant changes occur. In Fig. 6, we present the S_1-relaxed CAM-B3LYP potentials (light colours, cross markers). These excited PESs exhibit similar crossings to those observed for the S_0-relaxed case. However, a striking differ-
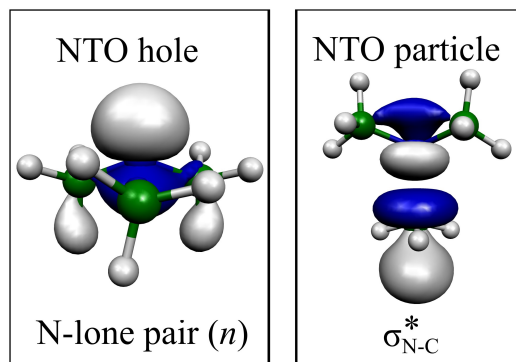
ence appears, as the intersection of S_1 and S_0 potentials at $R = 2.5$ Å. The reason for this S_1/S_0 intersection is ϑ-relaxation (planarisation) in the Rydberg states. The S_1-relaxed structures are planar ($\vartheta = 0$ deg.), at which, as seen from Fig. 3, the S_0 potential has a saddle point; this allows coupling with the S_1 PES, leading to a conical intersection. On the other hand, such coupling is not possible at the S_0-relaxed pyramidal geometry ($\vartheta \sim \pm 32$ deg.), which is why the S_1/S_0 (σ^*/GS) CI is missing in the PESs shown in Fig. 4. An additional effect of the S_1-relaxation is that it lowers the minimum of the excited-state potentials, relative to the one of the ground state, by $0.9 - 1.0$ eV, which is in good agreement with the calculated reorganization energy. This excess energy can be transformed into vibrational energy, initially concentrated in the ϑ mode. This means that the excited-state ensemble will likely be vibrationally hot.

The S_1-relaxed PESs shown in Fig. 6 stop at the $R = 2.5$ Å, because for higher R, the geometry relaxation does not converge. This is due to the failure of DFT, and in general, single-reference methods, to describe S_1/S_0 CIs. The problem is rooted in the erroneous description of the multiconfigurational ground state by a single Slater determinant. In order to obtain the DFT/TD-DFT potentials in the full 1 Å $\leq R \leq$ 5 Å space, we carried out a second set of calculations, for which the structures were generated from the optimised S_1 ($3s$) geometry, by changing R and keeping all other nuclear coordinates fixed; we refer to these potentials as the S_1- rigid PESs, which are also shown in Fig. 6 (normal colours). We assess the quality of these S_1 rigid potential curves by comparing them to CASPT2(6e,14o) PESs calculated for the same geometries, shown in Fig. 7. The result of this compari-
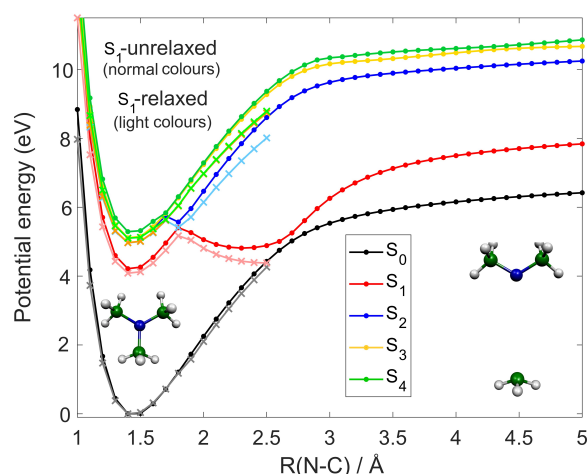
Fig. 6 Adiabatic PESs along R. The colors shown in the legend correspond to rigid PESs (structures generated from the optimised S_1 structure), while slightly modified colours (grey, pink, light blue, orange, and light green) and cross ("x") markers to relaxed equilibrium S_1 PESs ($\vartheta \sim 0$ deg.). Calculated at the CAM-B3LYP/aug-cc-pVDZ level of theory. The rigid structures at $R = 1.5$ Å and 5.0 Å are also shown.
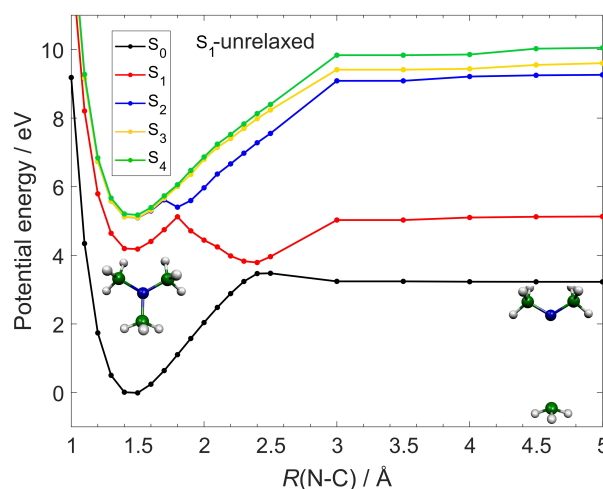

Fig. 7 Adiabatic rigid PESs along R. The utilised structures were generated from the optimised equilibrium S_1 geometry ($\vartheta \sim 0$ deg.). Calculated at the CASPT2(6e,14o)/aug-cc-pVDZ level of theory. The rigid structures at $R = 1.5$ Å and 5.0 Å are also shown.

son is that the CASPT2 excited-state crossings and barriers up to the S_1/S_0 conical intersection are well reproduced by TD-CAM-B3LYP; this qualifies the applied TD-DFT method for simulating dynamics occurring on the S_1–S_4 excited-state PESs. However, the S_1/S_0 intersection is displaced by $+0.2$ Å and more than 1 eV higher in energy, relative to the CASPT2 result. Furthermore, beyond the S_1/S_0 CI, the slight downhill in the CASPT2 S_0 potential is missing in DFT and the CAM-B3LYP dissociation curves flatten too slow and the energies at $R = 5$ Å are severely overestimated, by ca. 3 eV for the S_0 and S_1 states, in comparison to the CASPT2 ones. This is due to the erroneous description of static long-range (left-right) electron correlation in the applied DFT method. As seen in Sections 3.4 and 3.6, this deficiency of CAM-B3LYP will have a strong consequence for the simulated dissociation dynamics (dissociation yield).

3.3 Electronic population dynamics

We now present and analyse the TSH simulations of TMA, promoted to the $3p$ manifold. Out of the 156 trajectories, 128 (ca. 82%) were found to be excited to the S_4, 13 (ca. 8%) to S_3, and 15 (ca. 10%) to the S_2 state. Based on the electronic characters at time zero, the S_4 state always has dominant $3p_z$ character. Thus, the majority of the population is excited to the Rydberg $3p_z$ state with a minor $3p_x$, $3p_y$ component.

Fig. 8 presents the adiabatic population dynamics up to 3 ps, obtained by the CAM-B3LYP simulation. The obtained populations are converged with respect to the number of trajectories; this is confirmed by observing negligible changes when systematically decreasing the number of trajectories to be included in averaging the populations. In Fig. 8a, we summed up the populations of the S_2, S_3, and S_4 states (purple solid line) to estimate the $3p$ population. This is based on Fig. 6 and the analysis of electronic characters, which reveal that the S_2–S_4 adiabatic states mostly

preserve their $3p$ character along R (along the other nuclear coordinates, this adiabatic-diabatic correspondence is expected to be even better). In Fig. 8b, we show the $S_2/S_3/S_4$ populations separately. This shows that the excited-state population equilibrates very fast (~ 50 fs, see the inset of Fig. 8b) among the S_2–S_4 states, which is due to the energetic proximity and strong coupling of these three states. As a result of this strong coupling, the adiabatic S_2–S_4 states often have mixed $3p_x/3p_y/3p_z$ character. These results are in disagreement with the photoelectron spectroscopy study of Cardoza *et al.*, which led to a 540 ± 75 fs time constant for the $3p_z \rightarrow 3p_{x,y}$ internal conversion.[16] However, in this experiment, the excited-state population is generated by an off-resonant pump process, in contrast to the resonant excitation in our simulations, which is most likely the reason for the observed discrepancy,

The $S_2 + S_3 + S_4$ population decay in Fig. 8a is fitted excellently with a biexponential (purple dashed line in Fig. 8). From the fit, we find that the majority (66%) of the population decays with a 2.7 ps time constant, while the remaining minor component (34%) has a shorter 0.6 ps time constant. We interpret these population kinetics using the R-ϑ (here R is the longest N-C distance out of the three) distribution of all surface hops to the adiabatic S_1 state, shown in Fig. 9a, and the DFT/TD-DFT PESs in Figure 6. As can be seen in Fig. 9a, the hop histogram exhibit a double cluster structure; these two clusters represent a physical (56% of the hops, right cluster) and a non-physical (44% of the hops, left cluster) excited-state pathway. The right cluster is centered around $\vartheta = 0$ deg., $R = 1.80$ Å, corresponding to the S_2/S_1 ($\sigma^*/3s$) intersection. These hops are in line with electronic transitions happening in the region of strong nonadiabatic coupling (small energy gap), due to mixing with the dissociative σ^* state. The left cluster in Fig. 9a correspond to $3p \rightarrow 3s$ hops, occurring around $\vartheta = 0$ deg., $R = 1.50$ Å, i.e., the equilibrium excited-state geometry, where the $3p$-$3s$ energy gaps are large ($\sim 0.6 - 0.8$ eV). We note that hopping back from the S_1 ($3s$) to the S_2–S_4 ($3p$)
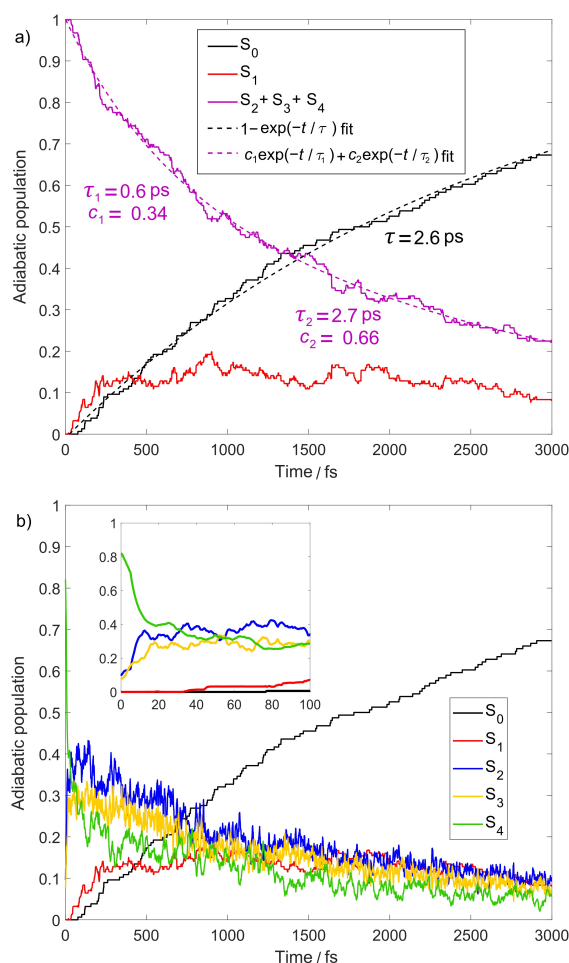
Fig. 8 Adiabatic populations (solid lines) for the CAM-B3LYP/aug-cc-pVDZ TSH dynamics, averaged over 156 trajectories. (a) S_2, S_3, S_4 populations summed up, the shown time constants were obtained by exponential fits (dashed lines). (b) S_2, S_3, S_4 populations shown separately. The inset shows zoom into the $t = 0 - 100$ fs interval.

Fig. 9 Histograms of the hops to the (a) S_1 and (b) S_0 state in the two-dimensional R-ϑ space. In the case of R, the longest out of the three N-C distances was selected. The electronic characters of the new state (to which the hop occurs) at the hopping geometries is also shown.

states also happens. Therefore, this mechanism does not lead to a net $3p \rightarrow 3s$ population transfer and cannot account for a physically observable internal conversion. We assign these transitions in the weak-coupling region as artefacts due to the approximate (stochastic) treatment of nonadiabatic effects in TSH, which fails for the non-crossing (weakly-coupled region).

Based on the above analysis, we assign the 0.6, 2.7 ps time constants of the $S_2 + S_3 + S_4$ population decay to the dynamics via the σ^*/Ryd conical intersections. From Fig. 6 and the right cluster in Fig. 9a, it is clear that these dynamics occur along the R(N-C) coordinate. We interpret this mechanism as follows. When TMA in the $3p$ states gains enough vibrational energy along R, it crosses the barrier and gains access to an excited-state pathway through the series of σ^*/$3p(3p_x)$, σ^*/$3s$, and σ^*/GS intersections. Analysis of the hops to S_1 around the S_2/S_1 (σ^*/$3s$) intersection (right cluster in Fig. 9a) reveals a branching with a dominant component towards decay to the S_0 state via the S_2/S_1 (σ^*/$3s$) conical intersection and a minor one (ca. 10%) to the $3s$. We mention that these two mechanisms were assumed in the
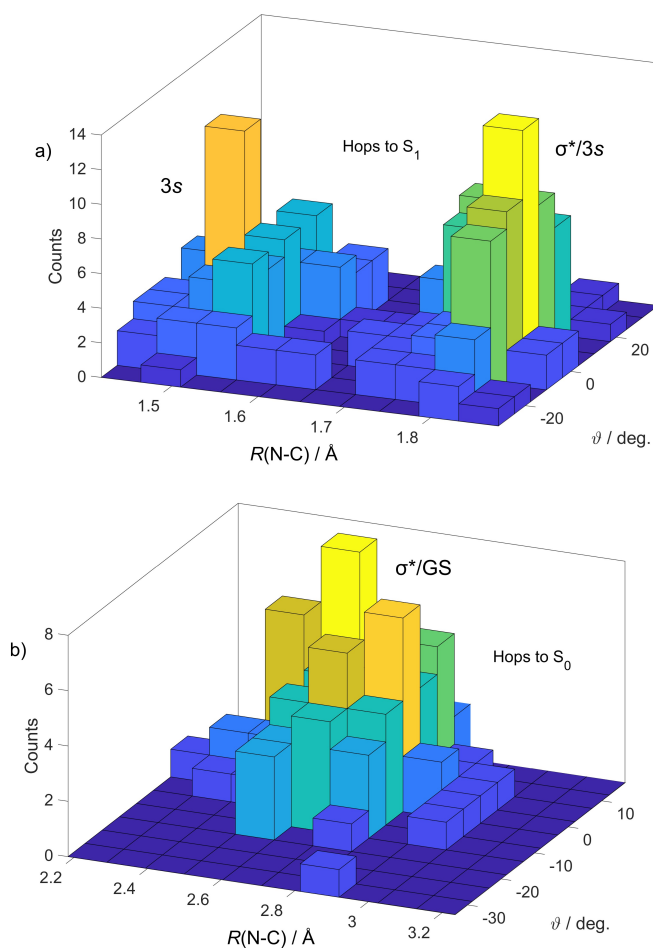
interpretation of the time-resolved X-ray scattering experiment of Ruddock *et al.*.[17] As seen in Fig. 6, the barrier along R for the $3s$ (S_1) state is significantly larger, nearly twice, as the one for the $3p$ states. Therefore, TMA can get trapped in the $3s$ state: this mechanism can thus account for net $3p \rightarrow 3s$ population transfer by internal conversion. In the photoelectron spectroscopy study of Cardoza *et al.*, $3p \rightarrow 3s$ IC is observed with a time constant of 2.9 ps, and no photodissociation is observed.[16] In this experiment, TMA was pumped at 209 nm, thus with smaller amount of excess vibrational energy, as in the 200 nm resonant case. It is therefore likely that, after IVR, TMA approaches the S_2/S_1 (σ^*/$3s$) intersection, at which the only energetically available pathway is towards the $3s$ minimum. This also explains why photodissociation is not observed in this experiment, as the dynamics might not energetically proceed towards the S_1/S_0 (σ^*/GS) intersection (note that this pathway is dominant in our simulations with excitation at resonance). Finally, we mention that in our TSH simulations, trapping in the $3s$ state does not occur, due to the discussed back-forward switching between the $3p$-$3s$ states.

We now focus on the dominant pathway towards the S_1/S_0 (σ^*/GS) conical intersection. After hopping to the S_1 state, these

trajectories very fast, in $15-30$ fs, reach the vicinity of the S_1/S_0 (σ^*/GS) intersection, where a hop to S_0 occurs. We here recall that we tackle the problematic description of the S_1/S_0 intersection by forcing an irreversible hop to S_0, when the S_1-S_0 energy gap reaches or exceeds the value of 0.15 eV. The short residence time on the S_1 (σ^*) surface explains why the red S_1 population curve in Fig. 8 remains low, and consequently, it predominantly reflects the $3s$ population. Fig. 9b displays the distribution of these hops in the 2D R-ϑ space. As seen in the figure, the distribution is centered at $R \sim 2.6$ Å, $\vartheta \sim 0$ deg., which is in excellent agreement with the intersection of the S_1-relaxed S_1/S_0 PESs shown in Fig. 6. The so-far presented results of the full-dimensional dynamics confirm that R and ϑ are the most important nuclear coordinates for the dynamics. Fig. 10 shows the temporal distribution (histogram) of the hops to S_0. This clearly reveals that the $S_1 \to S_0$ transition occurs on a faster ($0-1.5$ ps) and a slower ($1.5-3$ ps) timescale, which is in line with the two timescales identified by the biexponential fit of the $S_2 + S_3 + S_4$ population decay in Fig. 8a (0.6 ps and 2.7 ps exponential time constants). In Fig. 11, we show a representative trajectory for fast dynamics towards the S_1/S_0 intersection. As seen from the figure, TMA vibrates in the $3p$ manifold until ca. 80 fs, when it reaches the S_2/S_1 crossing region. Based on the PESs in Fig. 6, this is when the barrier in the $3p$ manifold is overcome, which enables the pathway along N-C bond stretching via σ^*/Ryd mixing, leading to a hop to the S_1 state. Afterwards, the trajectory propagates on the S_1 (σ^*) surface; during this time, the S_1 energy decreases, while the energy of the S_0, and S_2–S_4 states rises. Finally, the trajectory arrives to the S_1/S_0 intersection at ca. 120 fs. These results are in very good agreement with nonadiabatic dynamics on the PESs along R shown in Fig. 6. We note that the trajectories, in which a S_1/S_0 crossing occurs, exhibit a similar colenergy profile to the one shown in Fig. 11, and those, which do not have such crossing, are analogous to the non-crossing part of the trajectory in Fig. 11 (up to ca. 60 fs).
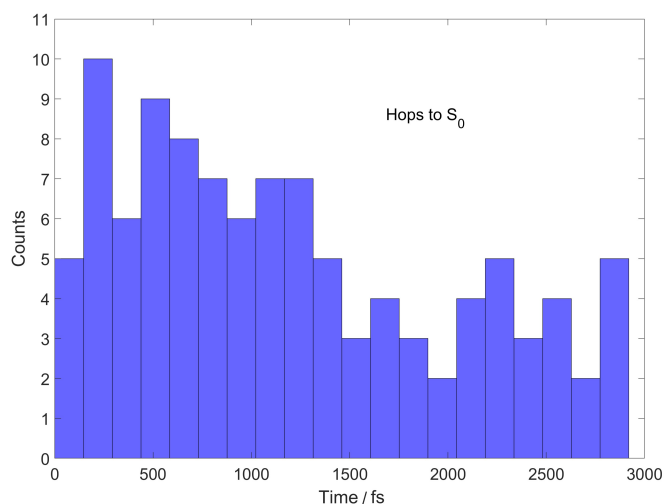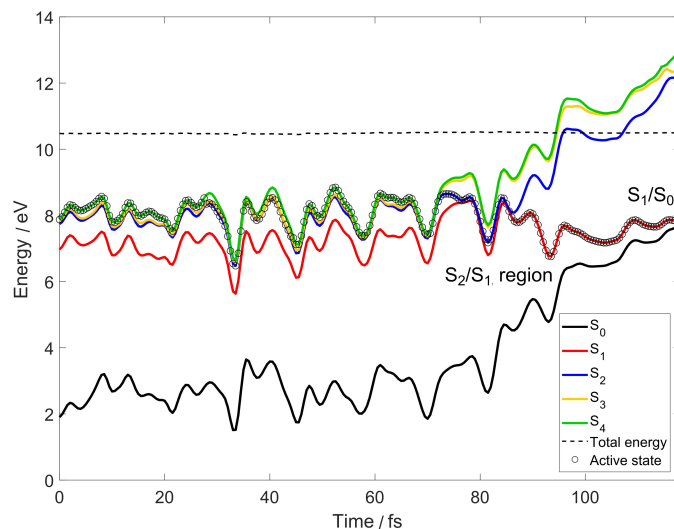

Fig. 11 Adiabatic state potential energies, total energy, and illustration of the active state for a representative trajectory undergoing ultrafast nonadiabatic dynamics.

Fig. 10 Time histogram of the hops to S_0.

We found above that the electronic population dynamics predominantly occurs along R. As the CAM-B3LYP and CASPT2 PESs

along R, shown in Figs. 6 and 7, respectively, up to the S_1/S_0 intersection, are in good agreement, we expect that the presented population dynamics are highly accurate. Note though that as described in Section 3.2, the CAM-B3LYP S_1/S_0 intersection lies slightly more than 1 eV above the CASPT2 one. Nevertheless, this should not have a significant effect on the population dynamics. Our results are also supported by the good general performance of CAM-B3LYP for Rydberg states, and specifically for TMA, the excellent agreement of vertical excitations between CAM-B3LYP and experimental values, as well as those calculated by higher level methods (EOM-CCSD, CASPT2). We further assess the quality of our dynamical results by comparison to time-resolved experiments. As discussed previously, the photoelectron spectroscopy study of Cardoza *et al.* does not allow such an assessment, due to the applied off-resonant excitation. On the other hand, in the X-ray scattering experiment of Ruddock *et al.*, resonant $3p$-excitation was employed, as is the case in our simulations; we here relate our so-far presented results to these experimental findings. Based on the PESs along R, arrival to the S_1/S_0 intersection can be interpreted as an indication that a photodissociation channel can potentially open up. Assuming $100-200$ fs for photodissocation to happen upon arrival to the S_1/S_0 conical intersection, the ~ 0.6 ps fast component of the simulated hops to the ground state (S_0) is in good agreement with the fast photodissociation observed experimentally with a 640 ± 130 fs time constant. This comparative analysis further supports the high quality of simulated nonadiabatic dynamics up to the arrival to the S_1/S_0 intersection. However, as seen in Section 3.2, the description beyond the S_1/S_0 intersection by CAM-B3LYP is erroneous, reflected by the severe overestimation of dissociation energy; we will return to this point in Sections 3.4 and 3.6.

3.4 Structural dynamics

We now analyse the structural dynamics along ϑ and R. Fig. 12a displays all 156 trajectories along ϑ and their time-dependent average $\langle\vartheta\rangle(t)$ (thick back line). As is clear from the figure, coherent oscillations are present in the first few hundred fs, the vibrational coherence then decays (decoherence). Vibrational dephasing is evident from Fig. 12a but amplitude loss due to internal vibrational energy redistribution cannot be ruled out either. We will return to these two damping mechanisms in Section 3.5. In Fig. 12b, we fit the mean $\langle\vartheta\rangle(t)$ with the function

$$f = A\cos(2\pi t/T)\exp(-t/\tau_d) , \qquad (3)$$

where A is fixed to $\langle\vartheta\rangle(0) = 32.1$ deg., T is the vibrational period, and τ_d is the damping time constant. As seen in Fig. 12b, we obtain $T = 104$ fs, leading to a $\nu = 321$ cm^{-1} vibrational frequency, and $\tau_d = 240$ fs. The 321 cm^{-1} value is in excellent agreement with TD-DFT-calculated $\nu = 321$ cm^{-1} frequency of the umbrella mode for the S$_2$ (3p_x), for S$_4$ (3p_z) it is $\nu = 339$ cm^{-1} (see the animation of the mode in the ESI). This reveals that the umbrella mode is excited by the UV pump, which is due to the sizeable nuclear gradient in the 3p states along ϑ at the ground-state equilibrium geometry (see Fig. 3). The oscillations are centered around $\vartheta \sim 0$ deg., which is where the Rydberg PES have their minimum, see Fig. 3. Coherent vibrations along the umbrella mode, and their dephasing, have indeed been observed experimentally for the related 3p-pumped cyclic amine N-methylmorpholine, using X-ray scattering[42]/photoelectron spectroscopy[43]. Here the -constant of the signal of ca. 635/520 fs, attributed to vibrational dephasing. For TMA, the decoherence dynamics are much faster, which is very likely the reason why it has not been observed by experiments with sub-ps time resolution.[16,17]

As seen above, the planarisation mode is excited and exhibits strong vibrational dynamics. However, this mode alone cannot account for nonadiabatic dynamics via σ^* mixing. The key to these, as is clear from our so-far presented results, is the N-C stretching coordinate, R. Thus, in the following, we analyse the structural dynamics along R. In Fig. 13, we show all 156 trajectories along R, here defined as the longest out of the three N-C distances, alongside with the time-dependent mean $\langle R\rangle(t)$. The figure demonstrates that the dynamics are dominated by bound N-C vibrations around the equilibrium value $R \sim 1.45$ Å. Apart from these, the only observable feature is an abrupt, ballistic N-C expansion. According to the PESs in Fig. 6, these ballistic dynamics are an indication of the discussed excited-state pathway through the conical intersections involving the dissociative σ^* state. The lag time during which only bound N-C vibrations occur, suggests an IVR mechanism for energy flow into the R nuclear coordinate. When enough energy is transferred to R, the barrier along R can be overcome, and very fast dynamics can occur, driven by the negative nuclear gradient (downhill in the PES, see Fig. 6). Finally, all trajectories that undergo ballistic N-C stretching dynamics end up in the S$_0$ state, upon arrival to the S$_1$/S$_0$ intersection. However, with the exception of two, these trajectories do not dissociate within the 3 ps time length of the simulations. In fact, they turn back almost instantaneously after
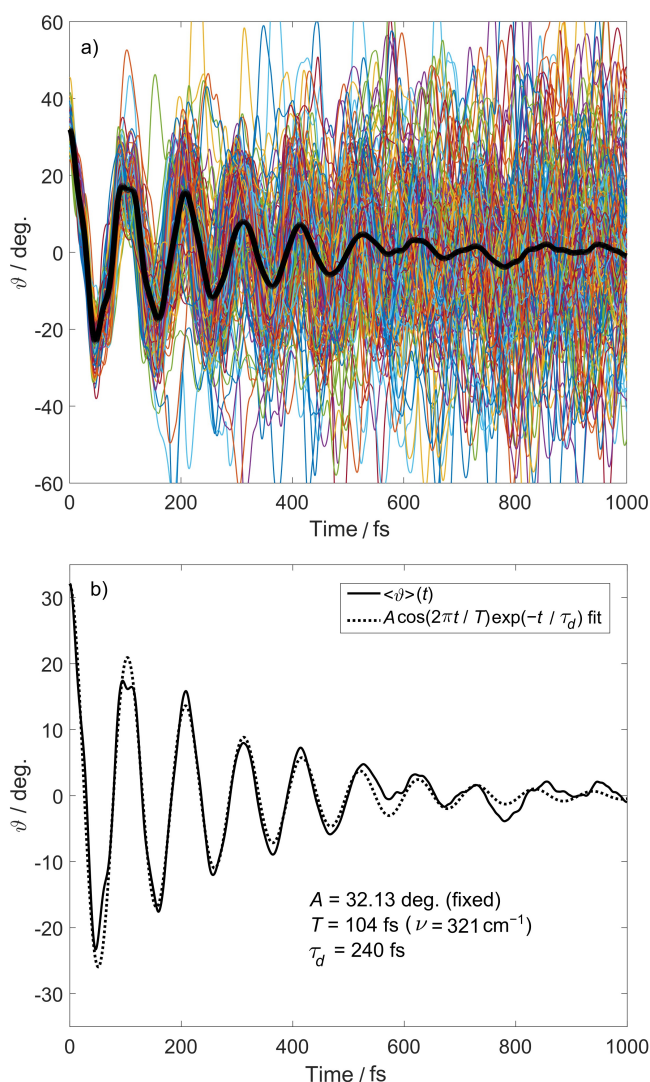

Fig. 12 (a) All 156 trajectories along ϑ, the thick black line shows the average $\langle\vartheta\rangle(t)$. (b) Fit of $\langle\vartheta\rangle(t)$ by an exponentially damped cosine function.

the ballistic N-C bond extension, at $R \sim 2.5 - 3$ Å. The reason for this is the erroneous description of dissociaton by the quantum chemistry method of our dynamical simulations, CAM-B3LYP. As discussed in Section 3.2, the CAM-B3LYP S$_0$ dissociation curve flattens slowly, leading to a too high dissociation energy, at least 3 eV higher than the on calculated by CASPT2 (see Figs. 6 and 7). Thus, after arrival to the S$_0$ surface, the kinetic energy along R rapidly runs out and the trajectories have to turn back towards the bound equilibrium geometry. The obtained 1% photodissociation yield at 3 ps is in sharp contrast with the corresponding experimental value of ca. 20%, confirming the deficiency of CAM-B3LYP to accurately describe N-C bond dissociation. On the other hand, a hypothetical case, in which all trajectories that transition to S$_0$ dissociate, would lead to a ca. 70% dissociation yield at 3 ps, also in disagreement with the experimental ca. 20% value. This analysis suggests that in the correct case, branching should occur at the S$_1$/S$_0$ intersection involving photodissociation and forma-
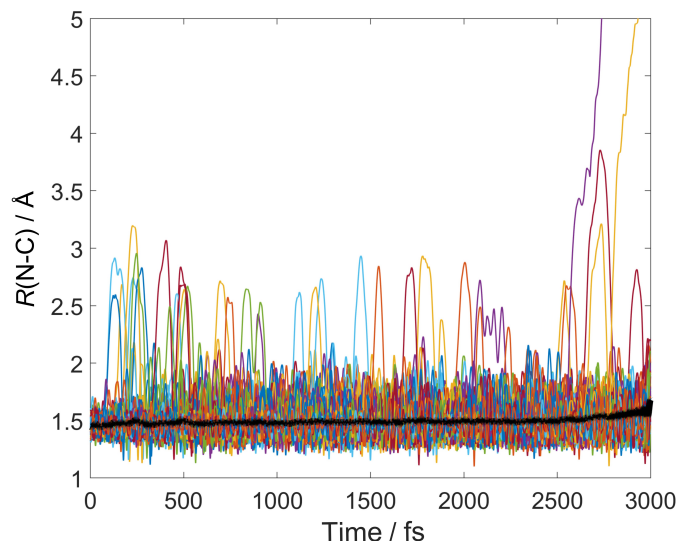
Fig. 13 All 156 trajectories along R, the thick black line shows the average $\langle R \rangle (t)$. R is defined here as the longest of the three N-C bond lengths.
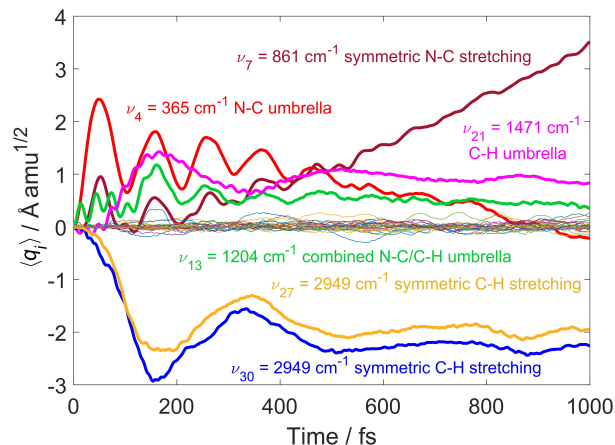

Fig. 14 Time-dependent structural dynamics, as obtained by projecting the nuclear displacement onto the ground-state mass-normal modes. The $\langle q \rangle (t)$ displacements in mass-weighted normal coordinates were averaged over all 156 trajectories. The vibrational frequencies ν_i and the character of the ground-state normal modes are also shown.

tion of hot GS bound TMA. In Section 3.6, we return to this point and show that pure DFT, i.e., GGA, without any Hartree-Fock exchange, is more suited for this problem. We therefore conclude here that our CAM-B3LYP TSH simulations are highly accurate, but only up to arrival to the S_1/S_0 conical intersection, after this point, it fails to describe photodissociaton. As a final note, we emphasise that the real problematic case here for CAM-B3LYP is not the description of the S_1/S_0 intersection, which is tackled by the strategy of irreversible forced hops, but the description of dissociation. This is confirmed by manually switching to S_0 at different energy gaps, leading to the same result: insufficient energy in R to dissociate.

3.5 Vibrational decoherence dynamics

A striking result of our simulated dynamics is the fast arrival to the S_1/S_0 conical intersection and thus ballistic N-C bond length expansion during the first ps; this is clearly observed in Fig. 13. These trajectories could potentially dissociate; this was indeed observed in the recent ultrafast X-ray scattering experiment of Ruddock *et al.*, even though this is not the case here due to erroneous electronic structure description of CAM-B3LYP at elongated N-C distances. Therefore, the excited-state mechanism enabling this fast channel is particularly intriguing; below we perform a normal mode analysis to investigate such mechanisms, which, in the present case, means vibrational decoherence dynamics.

In Fig. 14, we project the average nuclear displacements onto the ground-state normal modes, leading to $\langle q_i \rangle (t)$, the average time-dependent displacements in mass-weighted normal coordinates. $\langle q_i \rangle (t)$ is purely indicative of coherent vibrational motion, as random motion is cancelled out by the averaging. As expected, during the initial few hundred fs, the umbrella planarisation mode (labelled ν_4) exhibits the largest coherent motion. The red curve $\langle q_4 \rangle (t)$ shows analogous coherent oscillations with the same period and decay to the one of $\langle \vartheta \rangle (t)$ in Fig. 12. We find that during the decay, vibrational coherence is transferred

to other modes: two other umbrella modes with C-H (ν_{21}) and combined N-C/C-H (ν_{13}) wagging character, the symmetric N-C stretching mode (ν_7), as well as two symmetric C-H stretching modes (ν_{27} and ν_{30}), see the ESI for the animation of these modes. $\langle q_i \rangle (t)$ for modes ν_4, ν_7, and ν_{13} oscillates with the same ca. 100 fs period, which is assigned to the excited-state (Rydberg) N-C umbrella mode. This period for the higher frequency modes ν_{21}, ν_{27}, and ν_{30}, however, is significantly longer. ca. 360 fs. Although no ground-state normal mode has such long vibrational period, it matches with the period of excited-state (S_1 and S_2) C-H twisting. We note that this result can stem from the utilised projection technique to GS normal modes. As the observed vibrational coherence dynamics decays on similar timescales (within 0.6 ps) as the fast component of the electronic relaxation to the ground state occurs, these results are indicative of a mechanism, in which electronic relaxation and thus ballistic N-C stretching dynamics during the sub-ps open up due to vibrational coherence transfer and decoherence.

In the following, we examine the two mechanisms of vibrational decoherence: pure dephasing and energy transfer, i.e., IVR. From Figs. 12 and 14, it is evident that vibrational dephasing is operative during the first 500 fs but the role of possible IVR is unclear. We here extend our normal mode analysis for velocities; this leads to mass-weighted normal mode velocities $\dot{\boldsymbol{q}}(t)$ and the average kinetic energy $\langle E_{\mathrm{kin},i} \rangle (t) = 1/2 \langle \dot{q}_i(t)^2 \rangle (t)$, which allows to access energy transfer. In Fig. 15, we decompose the time-dependent average kinetic energy $\langle E_{\mathrm{kin},i} \rangle (t)$ into 4 groups, for different vibrational modes. The first group includes the three umbrella modes discussed above, ν_4, ν_{13}, and ν_{21}, with the obtained average kinetic energy displayed in red. Consistent with our observations, these modes acquire initially most of the vibrational energy due to the electronic excitation, via planaraization dynamics on the Rydberg PESs along ϑ. These 3 modes transfer ca. 0.4 eV vibrational energy to the bath of other vibrational modes of the molecule. We note that a very similar picture is seen when transforming the Cartesian kinetic energy for the internal

coordinate ϑ. Based on the energy content, and the oscillations in $\langle E_{\mathrm{kin},i}\rangle(t)$ during the first few hundred fs, the energy is transferred to 10 low-frequency (< 1300 cm^{-1}) C-H twisting/wagging and C-N stretching/bending modes (blue line, $v_1 - v_3, v_5 - v_{12}$). The energy is distributed evenly among these modes. In addition, we find a second energy transfer channel of ca. 0.3 eV from C-H stretching modes (orange line, $v_{25} - v_{33}$) to high-frequency (> 1300 cm^{-1}) C-H wagging and C-N bending/wagging modes. This energy dissipation exclusively occurs from antisymmetric C-H stretching modes. We note that this energy dissipation channel via C-H stretching modes can easily be a consequence of projection onto the GS normal modes; we expect dissipation through the umbrella modes to be dominant for the investigated IVR mechanism. Based on these results, we conclude that both vibrational decoherence mechanisms, pure dephasing and IVR are active during the first 500 fs; the latter enables fast electronic relaxation and ballistic N-C bond expansion by crossing the barrier along R in the $3p$ Rydberg states. We note that the sub-ps damping of oscillation amplitude in ϑ does, in fact, occur but is blurred in Fig. 12, when all trajectories are shown. On the longer ps timescale, all 4 classes of modes acquire vibrational energy (Fig. 15), which we attribute to conversion of potential to kinetic energy by electronic relaxation.
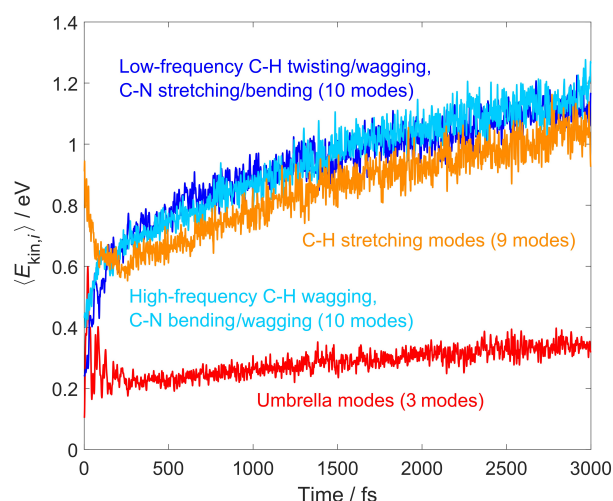

Fig. 15 Decomposition of the time-dependent average kinetic energy into 4 groups of vibrational modes: umbrella modes (red line, v_4, v_{13}, and v_{21}), low-frequency C-H twisting/wagging, C-N stretching/bending modes (blue line, $v_1 - v_3, v_5 - v_{12}$), high-frequency C-H wagging, C-N bending modes (light blue line, $v_{14} - v_{20}, v_{22} - v_{24}$), and C-H stretching modes (orange line, $v_{25} - v_{33}$).

3.6 Photodissociation dynamics

Finally, we return to the description of photodissociation by DFT. As discussed in Sections 3.2 and 3.3, it is clear that the dissociation energy at the CAM-B3LYP level is too high (see Fig. 6), which is the reason for the very low simulated dissociation yield (1%). It is known that the description of dissociation is governed by static electron correlation. CAM-B3LYP is a range-separated hybrid exchange-correlation functional with 65% Hartree-Fock exchange (HFx) and 35% DFT exchange (DFx) at long ranges.

HFx accounts for dynamical electron correlation, which increases the dynamical/static correlation ratio. Indeed, pure GGA functionals containing 0% HFx were found to be better for cases, for which static electron correlation is decisive, e.g., describing quasi-degeneracies.[44] The lack of static electron correlation at long range explains the failure of CAM-B3LYP to correctly describe dissociation. On the other hand, increased percentage of HFx at long range has crucial importance in the correct description of Rydberg states, for which, as also found in the present work, CAM-B3LYP performs excellently. In order to support these arguments, we carried out additional investigations using a pure GGA functional; for this we choose BLYP, which is the GGA-analogue of CAM-B3LYP. Fig. 16 shows the BLYP-calculated S_1- rigid PESs along R. In comparison to the CASPT2 (Fig. 7) and the DFT/TD-CAM-B3LYP (Fig. 6) PESs, the flattening of the dissociation curves is fast and the obtained S_0 dissociation energy, estimated at $R = 5$ Å, is only ca. 1 eV higher than the CASPT2 value, which is a significant improvement over the ca. 3 eV overestimaiton by CAM-B3LYP. However, the TD-BLYP Rydberg minimum energies are more than 1 eV lower than those calculated with CASPT2 and CAM-B3LYP. These results are in perfect agreement with our discussion on static-dynamical electron correlation. In order to examine how these changes manifest in the photodissociation dynamics, we have carried out additional TSH simulations using BLYP/aug-cc-pVDZ (124 trajectories). Fig. 17 displays all BLYP trajectories along R. In line with the lower dissociation energy, we observe more dissociating trajectories than for CAM-B3LYP, leading to ca. 6% and 23% dissociation yields at 1 ps and 3 ps, respectively, which is in excellent agreement with the experimental values of 10% (1 ps) and 20% (3 ps) of Ruddock et al..[17] The ps timescale of simulated photodissociation is in good agreement with the experimentally-observed fast photodissociation (640 fs time constant). Fig. 17 is indicative of a branching mechanism at the S_1/S_0 conical intersection: most trajectories fall back towards the bound equilibrium geometry but, in sharp contrast with the CAM-B3LYP simulations, here a considerable amount of trajectories do dissociate. These results confirm branching at the S_1/S_0 CI, forecasted by the analysis of Section 3.4. All dissociating trajectories dissociate after transition to S_0 when approaching the S_1/S_0 intersection. Although the dissociation dynamics is very different for the CAM-B3LYP and BLYP trajectories (i.e., the dissociation yield), the electronic state populations follow similar kinetics with ca. 70% S_0 population in both case at the final 3 ps time step of the simulations. Finally, an average N-C bond length of 1.46 Å and a CNC angle of 115 deg. is obtained for the hot dimethylamine radical, in excellent agreement with the experimental values of 1.45 ± 0.02 Å and 118 ± 4 deg.[17]

4 Conclusion

In this work, we present a computational study of TMA, photoexcited to the $3p$ Rydberg manifold, utilising electronic structure calculations and TSH dynamics simulations. Methodologically, in comparison to high-level *ab initio* (EOM-CCSD and CASPT2) results and experimental data, we find that the utilised TD-CAM-B3LYP method provides an accurate description of the Rydberg states; this is in agreement with previous studies.[20,21] Further-
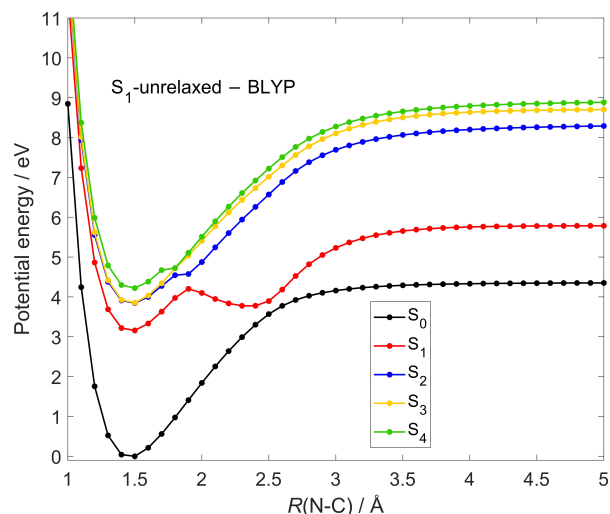
Fig. 16 Adiabatic S_1- rigid PESs along R. Calculated at the DFT/TD-BLYP/aug-cc-pVDZ level of theory. The utilised structures were generated from TD-BLYP-optimised S_1 geometry, i.e., $\vartheta \sim 0$ deg.
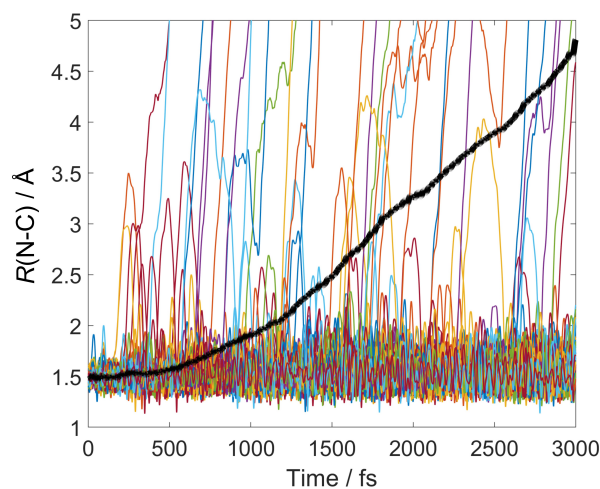

Fig. 17 All 124 BLYP trajectories along R, the thick black line shows the average $<R>(t)$. R is defined here as the longest of the three N-C bond lengths.

more, the approach of energy-based irreversible forced hops to S_0 made it possible to access the $S_1 \rightarrow S_0$ internal conversion by DFT/TD-DFT. TSH simulations based on CAM-B3LYP shed valuable insight into the excited-state dynamics of TMA. Upon photoexcitation into the $3p$ Rydberg states, TMA undergoes strong coherent vibrational dynamics along the planarisation mode, around the planar geometry. This is due to the removal of an electron from the nitrogen lone pair by the electronic excitation, eliminating the electronic repulsion, which makes the ground state of TMA pyramidal. The coherent oscillations have a period of 104 fs with a sub-ps coherence decay characterised by a 240 fs exponential time constant. Such coherent vibrational dynamics and decoherence have indeed been observed experimentally for N-methylmorpholine, [42,43] a cyclic amine with analogous Rydberg states; this has not been so far the case for TMA, most likely the fast vibration with ca. 100 fs period could not be re-

solved experimentally.

The planarisation dynamics along the umbrella angle ϑ dominates the nuclear motion in the Rydberg excited states. However, it does not allow nonadiabatic transitions, as the Rydberg character of excited states is preserved. We demonstrated that the Rydberg states mix with the dissociative σ_{N-C^*} state along the N-C stretching coordinate leading to a series of conical intersections ($\sigma^*/3p_x$, $\sigma^*/3s$, and σ^*/GS). In our TSH dynamics, we indeed observed nonadiabatic transitions around these intersections, leading to a ballistic N-C bond expansion up to ca. $2.5-3$ Å, where TMA enters the S_0 PES. The lag time for these ballistic dynamics and the coupled electronic relaxation dynamics via the dissociative σ^* state has two time scales: a faster (~ 1 ps) and a slower (~ 3 ps). This excited-state channel along the N-C stretching coordinate could potentially open up for photodissociation; the simulated sub-ps/ps timescales are in good agreement with the ones extracted from the fast experimental photodissociation component of ref. 17. However, only 1% of the trajectories did undergo dissociation within 3 ps, which is in disagreement with the experimental value of 20% at 3 ps. We attributed this failure to too high dissociation energy, resulting from the erroneous treatment of static electron correlation by CAM-B3LYP, which is due to the increased percentage of Hartree-Fock exchange at long range. We repeated the TSH simulations using BLYP, which is the GGA analogue of CAM-B3LYP. Although this led to worse description of the Rydberg states, it resulted in an increased dissociation yield (19%) that is in excellent agreement with the experimental yield (20%). This improvement is due to the better description of static correlation, resulting in a strong lowering of N-C dissociation energy (> 2 eV). Furthermore, with these simulations we gained access to the structure of the hot dimethyl amine radical, which agrees excellently with the one obtained by a recent ultrafast X-ray scattering experiment. [17]

In addition to the above discussed dominant channel via the σ^* state, we also observed a minor relaxation channel, identified as $3p \rightarrow 3s$ internal conversion. However, a significant portion of these transitions are most likely unphysical, arising due to the deficiency of TSH to correctly account for nonadiabatic effects in the weakly-coupled region. The remaining $3p \rightarrow 3s$ IC transitions appear as a minor component of the dominant pathway, via branching at the S_2/S_1 ($\sigma^*/3s$) conical intersection, thus in the presence of strong nonadiabatic coupling. We believe this is the most likely mechanism for the experimentally detectable internal conversion.

Finally, we investigated the activation mechanism of the N-C bond expansion dynamics. The broad distribution of lag times for ballistic N-C bond elongation suggests an IVR activation mechanism to overcome the barrier along R(N-C). Based on our normal mode analysis, we find evidence that the initially excited N-C umbrella mode transfers vibrational coherence to two other umbrella modes (combined N-C/C-H and C-H umbrella modes), and that significant energy transfer via decoherence occurs from these 3 umbrella modes to the bath of twisting/wagging/stretching modes, within 500 fs. This mechanism can enable efficient energy flow into the R(N-C) coordinate; indeed, we observed a high relative fraction of trajectories undergoing ballistic N-C bond elongation and crossing to the S_0 state on a similar timescale, which

supports this interpretation.

The present work illustrates the mutual character of nuclear-electronic coupling in the excited-state dynamics of TMA. Electronic excitation into Rydberg states induces strong coherent vibrational motion along the umbrella angle ϑ, whose decoherence dynamics, in turn, controls the electronic relaxation and ballistic dynamics along the N-C bond. These N-C stretching dynamics can potentially open up for photodissociaton, which is controlled by the branching at the S_1/S_0 conical intersection.

Conflicts of interest

There are no conflicts to declare.

Acknowledgements

Notes and references

1 *Applied Photochemistry*, ed. R. C. Evans, P. Douglas and H. D. Burrow, Springer Netherlands, 2013.

2 G. W. Crabtree and N. S. Lewis, *Phys. Today*, 2007, **60**, 37–42.

3 H. Zhang, Y. Lu, W. Han, J. Zhu, Y. Zhang and W. Huang, *Chem. Eng. J.*, 2020, **393**, 124766.

4 O. Kahn and C. J. Martinez, *Science*, 1998, **279**, 44–48.

5 A. Bousseksou, G. Molnár, L. Salmon and W. Nicolazzi, *Chem. Soc. Rev.*, 2011, **40**, 3313–3335.

6 H.-D. Meyer, U. Manthe and L. Cederbaum, *Chem. Phys. Lett.*, 1990, **165**, 73 – 78.

7 M. Beck, A. Jäckle, G. Worth and H.-D. Meyer, *Phys. Rep.*, 2000, **324**, 1 – 105.

8 M. Barbatti, *WIREs Comput. Mol. Sci.*, 2011, **1**, 620–633.

9 D. Bellshaw, R. S. Minns and A. Kirrander, *Phys. Chem. Chem. Phys.*, 2019, **21**, 14226–14237.

10 W. Xie, M. Sapunar, N. Došlić, M. Sala and W. Domcke, *J. Chem. Phys.*, 2019, **150**, 154119.

11 F. Plasser, R. Crespo-Otero, M. Pederzoli, J. Pittner, H. Lischka and M. Barbatti, *J. Chem. Theory Comput.*, 2014, **10**, 1395–1405.

12 M. Richter, S. Mai, P. Marquetand and L. González, *Phys. Chem. Chem. Phys.*, 2014, **16**, 24423–24436.

13 A. J. Atkins and L. González, *J. Phys. Chem. Lett.*, 2017, **8**, 3840–3845.

14 S. Mai and L. González, *Chem. Sci.*, 2019, **10**, 10405–10411.

15 J. P. Zobel, O. S. Bokareva, P. Zimmer, C. Wölper, M. Bauer and L. González, *Inorg. Chem.*, 2020, **59**, 14666–14678.

16 J. D. Cardoza, F. M. Rudakov and P. M. Weber, *J. Phys. Chem. A*, 2008, **112**, 10736–10743.

17 J. M. Ruddock, N. Zotev, B. Stankus, H. Yong, D. Bellshaw, S. Boutet, T. J. Lane, M. Liang, S. Carbajo, W. Du, A. Kirrander, M. Minitti and P. M. Weber, *Angew. Chem. Int. Ed.*, 2019, **58**, 6371–6375.

18 Y. Onitsuka, Y. Kadowaki, A. Tamakubo, K. Yamasaki and H. Kohguchi, *Chem. Phys. Lett.*, 2019, **716**, 28 – 34.

19 T. Yanai, D. P. Tew and N. C. Handy, *Chem. Phys. Lett.*, 2004, **393**, 51 – 57.

20 J. O. F. Thompson, L. B. Klein, T. I. Sølling, M. J. Paterson and D. Townsend, *Chem. Sci.*, 2016, **7**, 1826–1839.

21 M. D. J. Waters, A. B. Skov, M. A. B. Larsen, C. M. Clausen, P. M. Weber and T. I. Sølling, *Phys. Chem. Chem. Phys.*, 2019, **21**, 2283–2294.

22 S. Hirata and M. Head-Gordon, *Chem. Phys. Lett.*, 1999, **314**, 291 – 299.

23 J. P. Zobel, J. J. Nogueira and L. González, *Chem. Sci.*, 2017, **8**, 1482–1499.

24 F. Neese, *WIREs Comput. Mol. Sci.*, 2012, **2**, 73–78.

25 F. Neese, *WIREs Comput. Mol. Sci.*, 2018, **8**, e1327.

26 I. Fdez. Galván, M. Vacher, A. Alavi, C. Angeli, F. Aquilante, J. Autschbach, J. J. Bao, S. I. Bokarev, N. A. Bogdanov, R. K. Carlson, L. F. Chibotaru, J. Creutzberg, N. Dattani, M. G. Delcey, S. S. Dong, A. Dreuw, L. Freitag, L. M. Frutos, L. Gagliardi, F. Gendron, A. Giussani, L. González, G. Grell, M. Guo, C. E. Hoyer, M. Johansson, S. Keller, S. Knecht, G. Kovačević, E. Källman, G. Li Manni, M. Lundberg, Y. Ma, S. Mai, J. a. P. Malhado, P. Å. Malmqvist, P. Marquetand, S. A. Mewes, J. Norell, M. Olivucci, M. Oppel, Q. M. Phung, K. Pierloot, F. Plasser, M. Reiher, A. M. Sand, I. Schapiro, P. Sharma, C. J. Stein, L. K. Sørensen, D. G. Truhlar, M. Ugandi, L. Ungur, A. Valentini, S. Vancoillie, V. Veryazov, O. Weser, T. A. Wesołowski, P.-O. Widmark, S. Wouters, A. Zech, J. P. Zobel and R. Lindh, *J. Chem. Theory Comput.*, 2019, **15**, 5925–5964.

27 F. Aquilante, J. Autschbach, A. Baiardi, S. Battaglia, V. A. Borin, L. F. Chibotaru, I. Conti, L. De Vico, M. Delcey, I. Fdez. Galván, N. Ferré, L. Freitag, M. Garavelli, X. Gong, S. Knecht, E. D. Larsson, R. Lindh, M. Lundberg, P. Å. Malmqvist, A. Nenov, J. Norell, M. Odelius, M. Olivucci, T. B. Pedersen, L. Pedraza-González, Q. M. Phung, K. Pierloot, M. Reiher, I. Schapiro, J. Segarra-Martí, F. Segatta, L. Seijo, S. Sen, D.-C. Sergentu, C. J. Stein, L. Ungur, M. Vacher, A. Valentini and V. Veryazov, *J. Chem. Phys.*, 2020, **152**, 214117.

28 R. Crespo-Otero and M. Barbatti, *Chem. Rev.*, 2018, **118**, 7026–7068.

29 J. C. Tully, *J. Chem. Phys.*, 1990, **93**, 1061–1071.

30 G. Granucci, M. Persico and A. Toniolo, *J. Chem. Phys.*, 2001, **114**, 10608–10615.

31 F. Plasser, G. Granucci, J. Pittner, M. Barbatti, M. Persico and H. Lischka, *J. Chem. Phys.*, 2012, **137**, 22A514.

32 G. Granucci, M. Persico and A. Zoccante, *J. Chem. Phys.*, 2010, **133**, 134111.

33 Y. Mei and W. Yang, *J. Phys. Chem. Lett.*, 2019, **10**, 2538–2545.

34 M. Abedi, M. Pápai, K. V. Mikkelsen, N. E. Henriksen and K. B. Møller, *J. Phys. Chem. Lett.*, 2019, **10**, 3944–3949.

35 A. D. Becke, *Phys. Rev. A*, 1988, **38**, 3098–3100.

36 C. Lee, W. Yang and R. G. Parr, *Phys. Rev. B*, 1988, **37**, 785–789.

37 S. Mai, M. Richter, M. Heindl, M. F. S. J. Menger, A. Atkins, M. Ruckenbauer, F. Plasser, L. M. Ibele, S. Kropf, M. Oppel, P. Marquetand and L. González, *SHARC2.1: Surface Hopping Including Arbitrary Couplings — Program Package for Non-Adiabatic Dynamics*, sharc-md.org, 2019.

38 M. Richter, P. Marquetand, J. González-Vázquez, I. Sola and L. González, *J. Chem. Theory Comput.*, 2011, **7**, 1253–1258.

39 S. Mai, P. Marquetand and L. González, *WIREs Comput. Mol. Sci.*, 2018, **8**, e1370.

40 A. M. Halpern, M. J. Ondrechen and L. D. Ziegler, *J. Am. Chem. Soc.*, 1986, **108**, 3907–3912.

41 E. Tannenbaum, E. M. Coffin and A. J. Harrison, *J. Chem. Phys.*, 1953, **21**, 311–318.

42 B. Stankus, H. Yong, N. Zotev, J. M. Ruddock, D. Bellshaw, T. J. Lane, M. Liang, S. Boutet, S. Carbajo, J. S. Robinson, W. Du, N. Goff, Y. Chang, J. E. Koglin, M. P. Minitti, A. Kirrander and P. M. Weber, *Nat. Chem.*, 2019, **11**, 716–721.

43 Y. Zhang, H. Jónsson and P. M. Weber, *Phys. Chem. Chem. Phys.*, 2017, **19**, 26403–26411.

44 M. Pápai and G. Vankó, *J. Chem. Theory Comput.*, 2013, **9**, 5004–5020.